Chapter 6
Towards Time-Resolved Molecular Orbital Imaging

Masakazu Yamazaki, Tomoyuki Endo, Akiyoshi Hishikawa, and Masahiko Takahashi

Abstract Understanding the mechanism of a chemical reaction is essential for controlling selectivity and yields of products or designing a novel molecular function, which is one of the ultimate goals of chemistry. Since a chemical reaction can be defined as nuclear dynamics driven by the change in electron motion, time-resolved molecular orbital imaging would open the door not only to gain a deeper insight into molecular dynamics but also to advance and extend frontiers of science and technology. In this chapter, two experimental techniques that aim to visualize the changing molecular orbital pattern during a chemical reaction are described in detail. One is the attempt to tackle the issue in momentum space, and the other is the attempt to do the same based on laser tunneling ionization. It is demonstrated that these two techniques are each applicable to short-lived excited states, thereby both offering opportunities for investigating the driving force behind chemical reaction.

Keywords Molecular orbital · Electron Compton scattering · Tunneling ionization

M. Yamazaki
Department of Chemistry, School of Science, Tokyo Institute of Technology, Tokyo, Japan

T. Endo
Kansai Institute for Photon Science, National Institutes for Quantum Science and Technology, Kyoto, Japan

A. Hishikawa
Department of Chemistry, Graduate School of Science, Nagoya University, Nagoya, Japan

Research Center for Materials Science, Nagoya University, Nagoya, Japan

M. Takahashi (✉)
Institute of Multidisciplinary Research for Advanced Materials, Tohoku University, Sendai, Japan
e-mail: masahiko@tohoku.ac.jp

K. Ueda (ed.), *Ultrafast Electronic and Structural Dynamics*,
https://doi.org/10.1007/978-981-97-2914-2_6

6.1 Introduction

When a molecule in its ground state absorbs a photon of light of the appropriate wavelength, the molecule is raised to an electronically excited state. Such molecular excited states are usually short-lived, as they may subsequently undergo, within a short period of time, deactivation reactions involving isomerization, dissociation, radiative, nonradiative, and energy-transfer processes. Furthermore, since molecules in excited states are more reactive than those in their ground state, a lot and variety of chemical reactions in which molecular excited states participate can be found in literature. For these reasons, the study of excited-state molecular dynamics is a topic of growing interest owing to the fundamental importance as well as potential application in many areas [1].

The excited-state molecular dynamics or unimolecular chemical reaction can be regarded as a successive series of rearrangements of atoms in molecules. Since the molecular structure is continuously changing during the chemical reaction that often involves the breaking and formation of chemical bonds, several approaches to observe such nuclear dynamics in real time have been proposed and demonstrated in the last decades. From the most fundamental point of view, however, the nuclear dynamics is driven by the change of electron motion, so real-time observation of electron dynamics is essential to reaching one of the goals of chemistry, that is, complete understanding, control and design of a chemical reaction. Furthermore, if the frontier orbital theory [2] is applied to the electron dynamics, spatial pattern of the highest occupied molecular orbital (HOMO) of the transient, evolving system would serve particularly as the key to understanding of the direction and underlying mechanism of the chemical reaction. In this respect, it should be noted, on one hand, that there have not yet been any experimental techniques that enable one to look at molecular orbitals changing rapidly during chemical reaction. For instance, although the widely-used time-resolved photoelectron spectroscopy provides accurate information about binding energy values of the molecular orbitals of a transient system [3, 4], spatial patterns of the orbitals are beyond the reach of this experimental technique. On the other hand, quantum chemistry theory can, in principle, predict the direction and underlying mechanism of a chemical reaction as well as the spatial patterns of the orbitals by numerically integrating the time-dependent Schrödinger equation. However, such full quantum dynamics calculations are not practically feasible for systems having more than three atoms, due not only to computational cost problem but also to the difficulty in constructing the high-dimensional and coupled global potential energy surfaces. In order to overcome these theoretical impediments, the trajectory surface hopping method [5, 6] has been developed, but there is at present a severe limitation in the number of degrees of freedom that it can handle.

Under the above-mentioned situations, one may desire to have an experimental technique that makes it possible to look at molecular orbitals changing rapidly during a chemical reaction. The key for this challenge is to develop time-resolved versions of the existing molecular orbital imaging techniques such as $(e, 2e)$ electron momentum spectroscopy [7–13], laser tunneling imaging [14–24], and laser

high-order harmonics generation [25–28]. Indeed, such attempts have already been undertaken along that line, and they are the subject of this chapter. Here, two kinds of attempts are described. One is the method to tackle the issue in momentum space and the other is the method to do the same based on laser tunneling ionization. Their experimental principle and current status are discussed in Sects. 6.2 and 6.3, respectively. Finally, this chapter is concluded in Sect. 6.4.

6.2 Molecular Orbital Imaging in Momentum Space

6.2.1 (e, 2e) Electron Momentum Spectroscopy

Over the last five decades, electron momentum spectroscopy (EMS), also known as binary (e, 2e) spectroscopy, has been developed as a powerful means to provide unique and versatile information on the electronic structure and electron correlation effects in matter [7–13]. It is a kinematically complete high-energy electron-impact ionization experiment with large momentum transfer and large energy loss, in which both the inelastically scattered and ejected electrons are detected in coincidence. The (e, 2e) reaction that ionizes the target molecule M can be described by

$$\begin{array}{ccccccc} \mathrm{M} & + & \mathrm{e}_0^- & \rightarrow & \mathrm{e}_1^- & + & \mathrm{e}_2^- & + & \mathrm{M}^+ \\ & & (E_0, \boldsymbol{p}_0) & & (E_1, \boldsymbol{p}_1) & & (E_2, \boldsymbol{p}_2) & & (E_{\mathrm{recoil}}, \boldsymbol{q}) \end{array} \tag{6.1}$$

Here the E_j's and $\boldsymbol{p}_j$'s ($j = 0$, 1, and 2) are the kinetic energies and momenta of the incident, inelastically scattered, and ejected electrons, respectively. Similarly, E_{recoil} and $\boldsymbol{q}$ represent the recoil energy and recoil momentum of the residual ion M^+. Since the thermal energy of M as well as E_{recoil} is negligibly small compared with any of E_j's in the (e, 2e) reaction under consideration, one has the following conservation laws of energy and momentum,

$$E_{\mathrm{bind}} = E_0 - E_1 - E_2 \tag{6.2}$$

$$\boldsymbol{q} = \boldsymbol{p}_0 - \boldsymbol{p}_1 - \boldsymbol{p}_2. \tag{6.3}$$

Here, E_{bind} is the electron binding energy (ionization energy). Furthermore, since the experiment is performed under the high-energy Bethe ridge conditions [11, 13], where the collision kinematics most nearly corresponds to a collision of two free electrons with the residual ion M^+ acting as a spectator, the momentum of the target electron $\boldsymbol{p}$, before ionization, is equal in magnitude but opposite in sign to $\boldsymbol{q}$,

$$\boldsymbol{p} = -\boldsymbol{q} = \boldsymbol{p}_1 + \boldsymbol{p}_2 - \boldsymbol{p}_0. \tag{6.4}$$

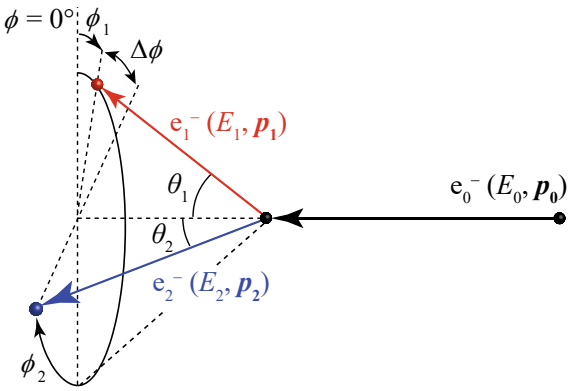

Fig. 6.1 Symmetric noncoplanar geometry for the study of the EMS reaction

The EMS signal can thus be measured as a function of E_{bind} and $\boldsymbol{p}$. Figure 6.1 shows the widely used symmetric noncoplanar geometry, in which two outgoing electrons having equal energies ($E_1 = E_2$) and making equal scattering polar angles ($\theta_1 = \theta_2 = 45°$) with respect to the incident electron beam axis are detected in coincidence. In this kinematic scheme, the magnitude of the target electron momentum $\boldsymbol{p}$ is given by

$$|\boldsymbol{p}| = \sqrt{(p_0 - \sqrt{2}p_1)^2 + (\sqrt{2}p_1 \sin(\Delta\phi/2))^2} \tag{6.5}$$

with $\Delta\phi$ being the out-of-plane azimuthal angle difference between the two outgoing electrons detected.

The most widely used scattering model for EMS is the plane-wave impulse approximation (PWIA) with the weak-coupling approximation [11, 12] that describes EMS cross-sections as

$$\frac{d^3\sigma_{\text{PWIA}}}{dE_1 d\Omega_1 d\Omega_2} \propto S_\alpha \frac{1}{4\pi} \int d\Omega |\psi_\alpha(\boldsymbol{p})|^2. \tag{6.6}$$

Here, $\psi_\alpha(\boldsymbol{p})$ is the momentum-space representation of the quasiparticle or Dyson orbital which can be defined as

$$\sqrt{S_\alpha}\psi_\alpha(\boldsymbol{p}) = \left\langle \boldsymbol{p}\Psi_f^{N-1} \,\middle|\, \Psi_i^N \right\rangle \tag{6.7}$$

Here, Ψ_i^N and Ψ_f^{N-1} are the N-electron initial neutral and the $(N-1)$-electron final ion wave functions of the target, and S_α is a quantity called pole strength, also known as the spectroscopic factor. $(1/4\pi)\int d\Omega$ is the spherical averaging due to random orientation of gaseous molecular targets.

In this way, EMS has a unique ability to measure momentum densities of each target electron with different binding energies or to look at individual molecular orbitals in momentum space. Since the position- and momentum-space molecular

orbital functions are uniquely related by the Dirac-Fourier transform, an expansion of a molecular orbital in position space corresponds to a contraction of it in momentum space. This is the material reason why EMS has proven sensitive to the behavior of the outer, loosely bound electrons that are of central importance in chemical properties such as bonding, reactivity, and molecular recognition.

6.2.2 Time-Resolved Electron Momentum Spectroscopy

EMS has a history since 1970s. Nevertheless, EMS experiments had long been limited to studies on stable targets in their electronic ground state, except the early pioneering experiment of Zheng et al. on excited sodium atoms prepared using a cw ring dye laser [29]. This is due partly to the difficulty of performing EMS experiments that require the coincident detection of the two outgoing electrons produced by high-energy electron-impact ionization at large momentum transfer, where the (e, 2e) cross-section is generally quite small compared with those at small momentum transfers. In addition, an ultrashort-pulsed incident electron beam, which is the primary requirement of conducting EMS experiments on short-lived transient species, may suffer from the space charge effect; the more intensity an ultrashort-pulsed incident electron beam has, the more space charge effect may significantly broaden not only the temporal width but also the energy spread of the electron packet. In this respect, however, highly encouraging was continuing efforts for progress of the EMS experimental techniques [7–13], one of which has eventually improved the instrumental sensitivity as much as possible [30, 31] by covering almost completely the available azimuthal angle range for the symmetric noncoplanar EMS reaction (Fig. 6.1). Under these circumstances, time-resolved EMS (TR-EMS) has been proposed in 2008 [13], and the first-generation apparatuses [32–34] have been developed recently.

Figure 6.2 shows a schematic picture of the experimental setup employed in the first TR-EMS apparatus [32]. The 800 nm output of a 5-kHz femtosecond laser (<120 fs, 0.8 mJ) is split into a pump path and an electron-generation path. 90% of the output is used to yield with an optical parametric amplifier the pump laser pulse (195 nm, ~120 fs, 0.8 μJ), which is subsequently used to excite target molecules in an effusive gas beam after the 5-kHz repetition rate being halved by an optical chopper. On the other hand, 10% of the 800 nm output is frequency tripled (267 nm, <10 μJ) and directed toward a back-illuminated photocathode in order to produce electron pulses via the photoelectric effect. The photocathode is made of a silver film of 40 nm thickness, which is negatively biased to accelerate the electron pulses up to 1.2 keV. The resulting ultrashort pulsed electron beam (~1 ps, ~50 pA) is then used to induce EMS events which are recorded by an EMS spectrometer with an exceptionally large spherical analyzer (mean radius of 220 mm). The energy- and momentum-dispersive multichannel measurement is achieved based on the well-known property of a spherical analyzer of maintaining the azimuthal angles of the analyzed electrons while dispersing them according to their kinetic energies. The delay time t_{delay} between the arrival of the pump laser pulse and the probe electron

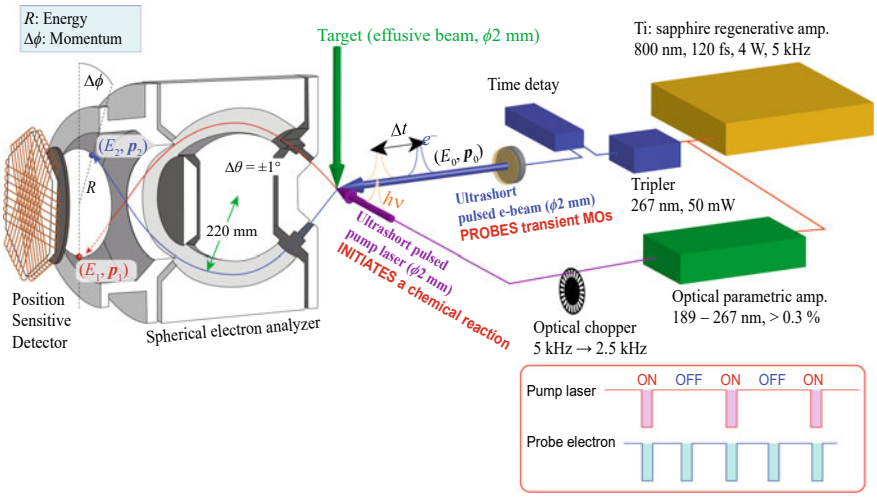

Fig. 6.2 A schematic representation of time-resolved electron momentum spectroscopy apparatus [32]

pulse is controlled with a computer-driven translation stage. Here, in order to have a workable signal count rate, diameters of the target gas beam, the pump laser, and the probe electron beam are all set to be about 2 mm, at the expense of the experimental resolutions for the energy (5 eV FWHM), momentum (0.4 a.u. at $\Delta\phi = 0°$), and time ($\pm$35 ps). Note that the time resolution is almost entirely dominated by the group velocity mismatch between the pump laser and probe electron pulses [35]. Note also that since the 5 kHz repetition rate is halved only for the pump laser, the TR-EMS apparatus concurrently produces two kinds of EMS data sets. One is data that are measured with the pump laser (laser-on), the other is reference data that are measured without the pump laser (laser-off). The TR-EMS data are then obtained by subtracting the laser-off spectrum with an appropriate weight factor from the laser-on spectrum.

6.2.3 *TR-EMS Study on the S_2 Acetone*

The first application of TR-EMS to a molecular excited state has been made for the deuterated acetone molecule (acetone-*d*6), $(CD_3)_2CO$, in its second excited singlet $S_2(n, 3s)$ state [36] with a lifetime of 13.5 ps [37]. Figure 6.3a compares the laser-off binding energy spectrum with an associated theoretical spectrum for the acetone-*d*6 ground state. It can be seen that although the employed instrumental energy resolution of 5 eV FWHM does not allow the spectral peaks to be identified clearly, the laser-off spectrum is on the whole well reproduced by the associated theoretical spectrum over the entire binding energy range covered.

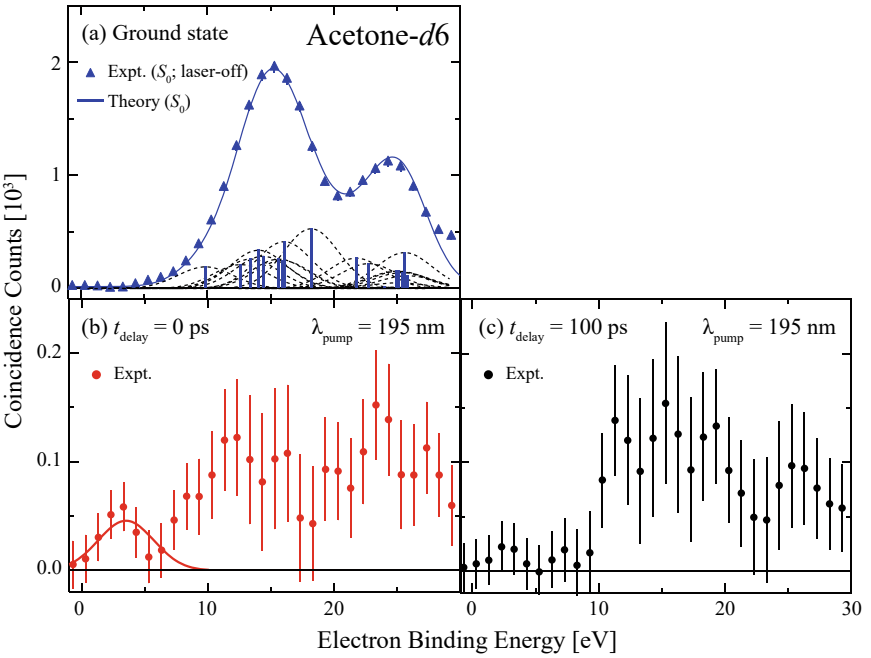

Fig. 6.3 Experimental **a** laser-off EMS binding energy spectrum and time-resolved EMS binding energy spectra of the acetone-*d*6 S_2 state obtained at t_{delay} of **b** 0 ps and **c** 100 ps. The broken and solid lines for **a** represent associated theoretical calculations. The solid line for **b** represents a band due to ionization from the outermost 3*s* Rydberg orbital. Adapted with permission from Ref. [36]. Copyright 2015 by American Physical Society

Figure 6.3b shows a TR-EMS binding energy spectrum of the acetone-*d*6 S_2 state at 195 nm, measured at $t_{delay} = 0$ ps. It is evident from Fig. 6.3b that a band appears at around $E_{bind} = 3.5$ eV which is undoubtedly assigned, from the energy conservation, to ionization from the HOMO (outermost 3*s* Rydberg orbital) of the acetone-*d*6 S_2 excited state. Furthermore, the 3.5 eV band disappears when t_{delay} is changed from 0 to 100 ps, as can be seen from Fig. 6.3c. This is indeed in accordance with the fact that the acetone-*d*6 S_2 state has a lifetime of 13.5 ps, and it undergoes the three-body ultrafast dissociation process to eventually produce $2CD_3$ and CO [37], indicating that the $t_{delay} = 100$ ps spectrum is largely governed by the reaction products.

Further evidence for the successful measurement is given by examining the electron momentum distribution for the 3.5 eV band. Figure 6.4 shows spherically averaged electron-momentum-density distribution for the 3 s Rydberg orbital, which was constructed by plotting the number of true coincidence events that formed the 3.5 eV band as a function of the electron momentum. Also included in the figure are associated theoretical distributions calculated for an empty 3 s Kohn–Sham orbital (DFT_3s Ryd.) of the acetone-*d*6 S_0 state or a 3*s* orbital of the S_2 state optimized with the

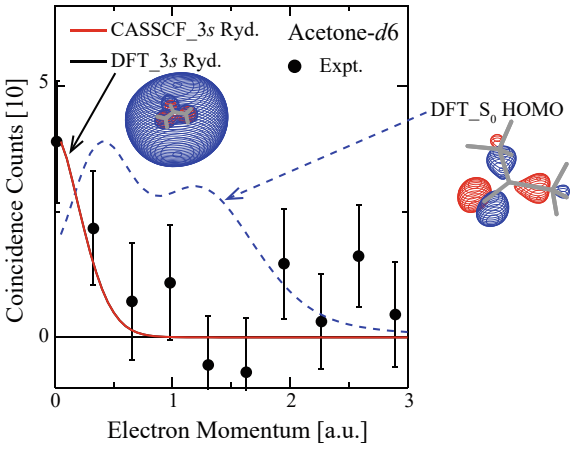

Fig. 6.4 Comparison of spherically averaged electron momentum-density distributions between experiment and theory for the 3*s* Rydberg orbital of the acetone-*d*6 S_2 state. Adapted with permission from Ref. [36]. Copyright 2015 by American Physical Society

complete-active-space self-consistent-field method (CASSCF_3s Ryd.). A theoretical distribution for the HOMO of the S_0 state (DFT_S_0 HOMO) is also included as a reference.

It can be seen from Fig. 6.4 that the experimental result exhibits a maximum at the momentum origin and its intensity drops off rapidly with the increase in the electron momentum. This behavior can be understood by considering in momentum space the nature of the 3*s* Rydberg orbital. Since the angular part of a wavefunction is invariant under the Dirac-Fourier transform, a certain molecular orbital in position space has similar shape in momentum space. On the other hand, the radial part of a wave function is largely affected by the Dirac-Fourier transformation; high density at large *r* leads to high density at small *p* and vice versa. Thus, the diffuse 3 s Rydberg orbital in position space possesses the sharply peaked momentum distribution. The associated theoretical calculations support this observation. This achievement can thus be recognized as having demonstrated that EMS measurements of short-lived molecular excited states are certainly feasible [38, 39].

6.2.4 TR-EMS Study on the S_1 *Toluene*

The first molecular orbital imaging experiment for a molecular excited state discussed in Sect. 6.2.3 [36] is not enough to show the potential capability of TR-EMS; its observation was limited only to the energetically well-separated HOMO of the acetone S_2 state. TR-EMS should be able to observe spatial distributions, in momentum space, of not only the HOMO but also all other, more tightly bound orbitals of a molecular excited state. The limitation in the first TR-EMS experiment [36] is due to the fact that the acetone S_2 state decays faster than the employed time resolution (±35 ps). Thus, the experiment on the higher-binding-energy region shown in Fig. 6.3b had to be affected by its subsequent decay process. The potential capability of TR-EMS to

observe individual orbitals of a molecular excited state has then been demonstrated by changing its target to the toluene molecule in the $S_1(\pi, \pi^*)$ state at 267 nm [40]. Since the toluene S_1 state has a lifetime of 86 ns [41], much longer than the time resolution of ± 35 ps, a TR-EMS experiment without any contributions of the subsequent intramolecular relaxation processes can be made while the whole valence electronic structure must be observed in the binding energy spectrum.

Figure 6.5a, b shows TR-EMS binding energy spectra obtained for the toluene S_0 (ground) and S_1 (excited) states, respectively. The former is the laser-off spectrum, while the latter was obtained at $t_{\text{delay}} = 0$ ps. Also included in the figures are associated theoretical spectra calculated by using the symmetry adapted cluster configuration-interaction (SAC-CI) method [42]. It can be seen from Fig. 6.5a that the employed instrumental energy resolution of 5 eV FWHM only allows the spectral peaks to be identified as two broad bands centered at around 14 and 24 eV, which are a group of peaks due to the outer-valence and inner-valence ionization, respectively. It is also seen that the experiment is on the whole well reproduced by the theoretical spectrum over the entire binding energy range that the SAC-CI calculations covered.

As for the S_1 spectrum in Fig. 6.5b, there are two additional features. One is the appearance of a very weak band at a lower binding-energy region centered at 4–5 eV which is assigned to the ionization from the excited π^* orbitals of the toluene S_1 state. The weak band intensity originates mainly in the electron occupation number. Indeed, the SAC-CI wave function of the toluene S_1 state can be approximated as a linear combination of two electronic configurations, $0.70 \times [(3\pi)^{-1}(1\pi^*)^1] + 0.63$

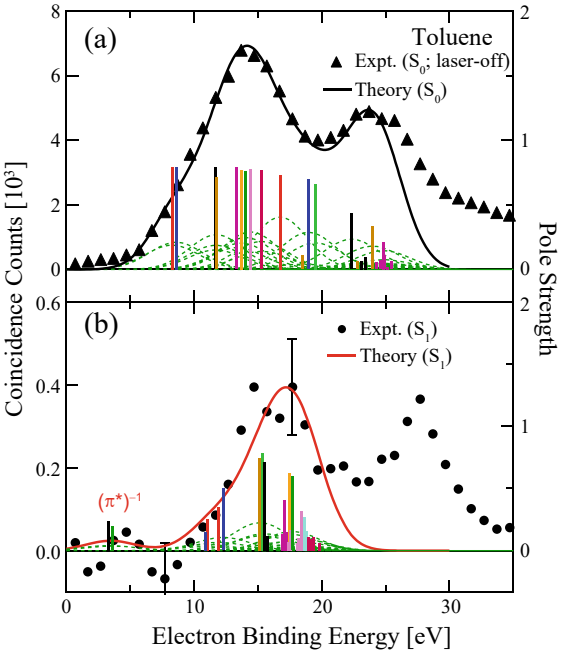

Fig. 6.5 Comparisons of binding energy spectra between the experiments and SACCI calculations for the **a** S_0 and **b** S_1 states of toluene. The dashed lines show the contribution of each transition and the solid line is their sum. Vertical bars represent pole strength (>0.05). Reprinted with permission from Ref. [40]. Copyright 2016 by American Physical Society

$\times [(2\pi)^{-1}(2\pi^*)^1]$ in which the two $1\pi^*$ and $2\pi^*$ excited orbitals are almost equally occupied by one electron. Thus, the energetically close-lying transitions from the S_1 state to the ground ($D_0[(3\pi)^{-1}]$) and first excited ($D_1[(2\pi)^{-1}]$) states of the toluene cation appear with small pole strength values.

Another feature of the S_1 spectrum in Fig. 6.5b is a shift of both the outer- and inner-valence bands towards higher energy by about 3 eV compared to those at ~14 and ~24 eV in the S_0 spectrum. This observation can be understood by extending the ionization propensity rule of EMS to molecular excited states. Namely, only one-electron processes are allowed, but two-electron and other multi-electron processes are all forbidden. For instance, as shown in Fig. 6.6, the ionization to the $D_2[(15\sigma)^{-1}]$ state is forbidden from the S_1 state, as it is a two-electron process, whilst it is allowed from the S_0 state. On the contrary, transitions from the S_1 state to higher-energy ionic states of two-hole-one-particle ($2h1p$) configurations such as $[(15\sigma)^{-1}(3\pi)^{-1}(1\pi^*)^1]$ and $[(15\sigma)^{-1}(2\pi)^{-1}(2\pi^*)^1]$ are allowed, although those from the S_0 state are forbidden. The same argument can be made for all other, more tightly bound molecular orbitals. It was found from the SAC-CI calculations that most of the allowed $2h1p$ configurations have the $1\pi^*$ or $2\pi^*$ orbital occupied by an electron. Thus, the outer- and inner-valence ionization bands of the S_1 state are expected to shift towards higher energy approximately by the difference in the π–π^* excitation energy between the S_0 and D_0 states, i.e., $E^{D_0}_{\pi\pi^*} - E^{S_0}_{\pi\pi^*}$, respectively. The calculated value for $E^{D_0}_{\pi\pi^*} - E^{S_0}_{\pi\pi^*}$ is 2.9 eV, and this is in good agreement with the experimental value of ~3 eV.

Note that the critical role of $2h1p$ configurations is an indication of the inherent capability of TR-EMS of being able to observe spatial distributions, in momentum space, of not only the HOMO but also all other, more tightly bound orbitals of a molecular excited state. This is because in primary ionization to such a $2h1p$ configuration the Dyson orbital is always of either the fully occupied orbitals or the singly occupied orbital of lower energy, which could be separately observed if the energy resolution were improved to the desired extent.

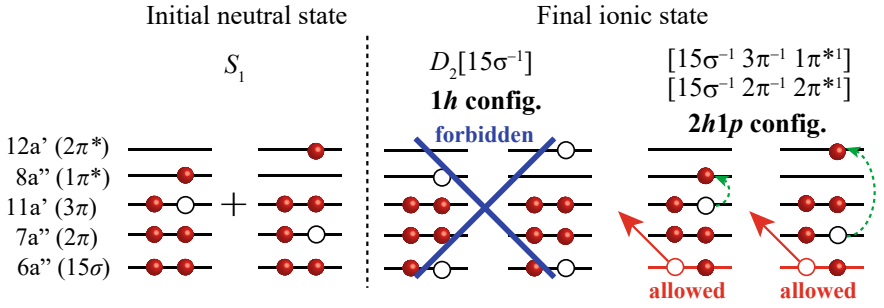

Fig. 6.6 EMS ionization schemes for transitions from the toluene S_1 state to several ionic states within the frozen orbital approximation, showing their occupation with electrons (closed circles) or holes (open circles). Adapted with permission from Ref. [40]. Copyright 2016 by American Physical Society

6.3 Molecular Orbital Imaging by Ultrafast Laser Tunneling

Thanks to recent developments in laser technology, it is now possible to generate ultrashort intense laser fields from a table-top laser system. Due to the large electric fields, molecules in intense laser fields show a variety of characteristic features that are hardly observable in a weak field regime. In this section, we describe an approach to visualize electron distributions in molecules by utilizing one of such processes, laser tunneling ionization. The application to electronically ground and excited molecules is presented with illustrative examples on a small molecule, nitric oxide (NO) [23, 24].

6.3.1 Laser Tunneling Ionization

When molecules are exposed to intense laser fields (typically ~10^{14} W/cm^2), the electron binding potential is deformed due to the large electric fields as shown in Fig. 6.7a. The electron tunnels through a potential barrier thus formed into continuum states. This ionization process is called "laser tunneling ionization". The tunneling electron comes mainly from the outermost molecular orbital, typically HOMO, which has a thinner potential barrier than lower lying molecular orbitals such as HOMO-1 and HOMO-2. The rate of laser tunneling ionization depends on the shape of molecular orbital along the laser polarization direction. When the lobes of a molecular orbital face the laser polarization direction, the tunneling ionization is expected to be enhanced because of the large electron densities along the laser polarization direction. Since HOMO of NO has the π symmetry, the tunneling ionization is expected to become prominent when the molecular axis is oriented at 45° with respect to the laser polarization direction as shown in Fig. 6.7b. On the other hand, when the laser electric fields are applied along the nodes, the tunneling ionization should be suppressed due to small electron densities. This corresponds to the parallel orientation of the NO molecular axis (Fig. 6.7c). Thus, the angular dependence of laser tunneling ionization reflects the electron distribution in the molecular frame, or the shape of the molecular orbital. This feature is examined by various theoretical approaches [43–47], and the roles of various factors in tunneling ionization such as the permanent dipole moment, distortion of molecular orbital, and contributions from the lower lying orbitals are discussed.

There are several experimental approaches to obtain the angular dependence of ionization probability. For aligned or oriented molecules, it can be obtained as a function of the polarization direction of laser fields in the laboratory frame [14–16]. Alternatively, electron–ion coincidence momentum measurements can be used for randomly oriented molecules, to record molecular frame photoelectron angular distribution in circularly polarized laser fields [17–19]. Laser high-order harmonics

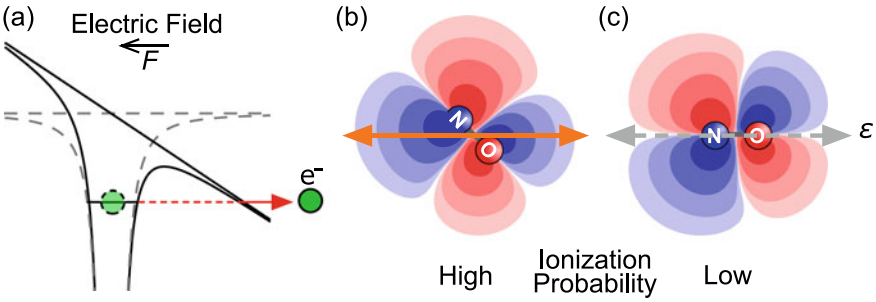

Fig. 6.7 **a** Schematic of laser tunneling ionization. Field-free electron binding potential (grey broken line) is deformed by applying external electric field F. Electron tunnels through the potential barrier (black solid line). **b**, **c** Orientation dependence of tunneling ionization probability of NO with respect to the laser polarization direction ε. Tunneling ionization rate of **b** 45° oriented configuration is higher than that of **c** parallel configuration due to π symmetry of the HOMO of NO

generation by recombination of tunneling electron to the parent ion is another interesting approach capable of determining phase of molecular orbitals [25–28]. Here, we employ ion momentum imaging of fragment ions produced by dissociative ionization or Coulomb explosion [20–24]. As illustrated in Fig. 6.7b, c, tunneling ionization of a molecular orbital determines the alignment or orientation of the resultant molecular ions. Thus, it is possible to capture the orbital shape from the fragment angular distribution under the axial recoil approximation. The simple experimental setup allowed us to explore the application of laser tunneling ionization imaging to molecular photoexcitation.

6.3.2 *Tunneling Ionization Imaging of NO 2π orbital*

First, we discuss tunneling ionization imaging on NO in the $X^2\Pi$ ground state, where the electric configuration is $(1\sigma)^2\ (2\sigma)^2\ (3\sigma)^2\ (4\sigma)^2\ (5\sigma)^2\ (1\pi)^4\ (2\pi)^1$. The experimental setup is shown in Fig. 6.8. Briefly, a linearly polarized intense laser pulse is focused onto a molecular beam of NO introduced into an ultrahigh vacuum chamber (residual gas pressure $\leq 10^{-7}$ Pa). Ions generated by dissociative ionization of NO, $NO \rightarrow NO^+ + e^- \rightarrow N^+ + O + e^-$, are detected by a position-sensitive detector (PSD) [48]. The three-dimensional momentum vector $\mathbf{p} = (p_x, p_y, p_z)$ of each ion is calculated using the arrival time (t) and position (x, y) at the detector.

The N^+ momentum image in one-color intense laser fields (45 fs, 800 nm, 1×10^{14} W/cm^2) is shown in Fig. 6.9a. The N^+ momentum image shows a clear butterfly-like pattern peaked at 40 and 140° with respect to the laser polarization direction, as expected from the shape of the 2π HOMO (see Fig. 6.7). The molecular dissociation subsequent to the tunneling ionization ejects the fragment ion with an offset angle against the laser polarization direction.

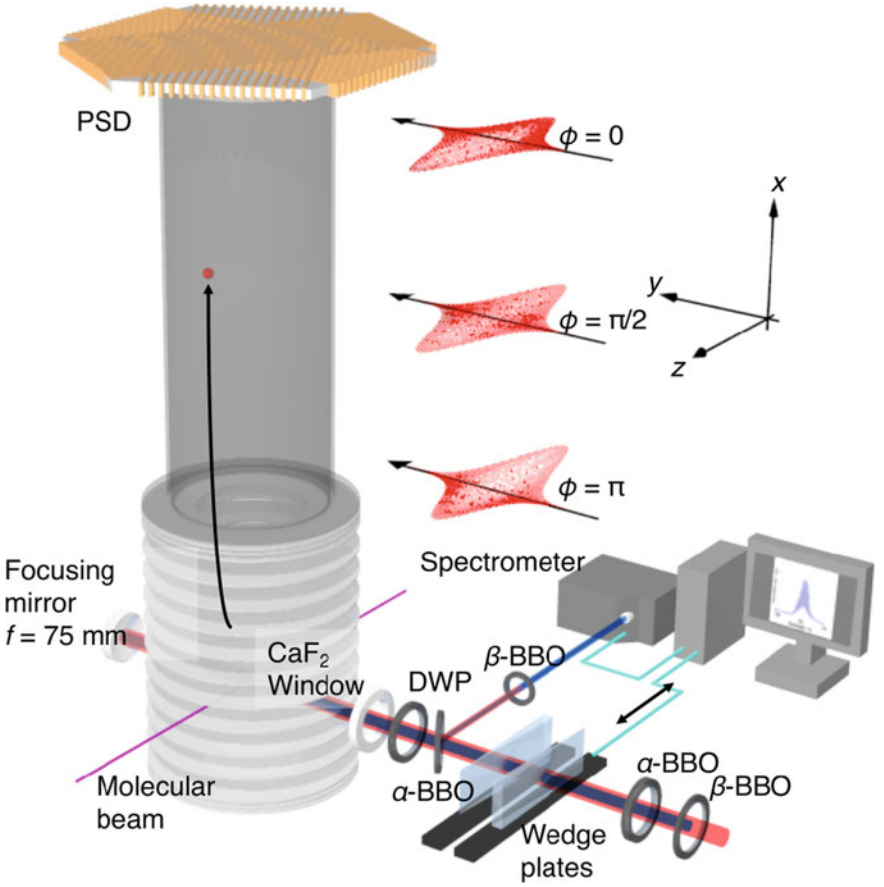

Fig. 6.8 Schematic of the experimental setup with phase-locked two-color laser pulses. The fundamental femtosecond laser pulse (45 fs, 800 nm, 1 kHz) and the second harmonics generated by a β-barium borate (BBO) crystal are co-linearly introduced to the three-dimensional ion momentum imaging spectrometer. The time delay between ω and 2ω pulses is controlled by birefringent α-BBO crystal and a pair of fused silica wedges. The relative phase is locked by a feedback loop utilizing the 2ω–2ω interference spectrum [50, 51]. The fragment ions produced from the interaction region are guided by a uniform electric field (61 V/cm) to reach a PSD through a field-free region. Temporal profiles of the two-color laser electric fields for the relative phases of 0, $\pi/2$, and π are shown in the subset. DWP: dual-wavelength wave plate; PSD: position-sensitive detector. Adapted with permission from Ref. [24]. Copyright 2019 by American Physical Society

Shown in Fig. 6.9b is the N^+ image obtained with asymmetric two-color laser fields [24], generated by a coherent superposition of the fundamental and second harmonic laser pulses [49–52]. The two-color laser electric field may be expressed as

$$F(t) = F_{\omega}(t)\cos(\omega t) + F_{2\omega}(t)\cos(2\omega t + \phi), \tag{6.8}$$

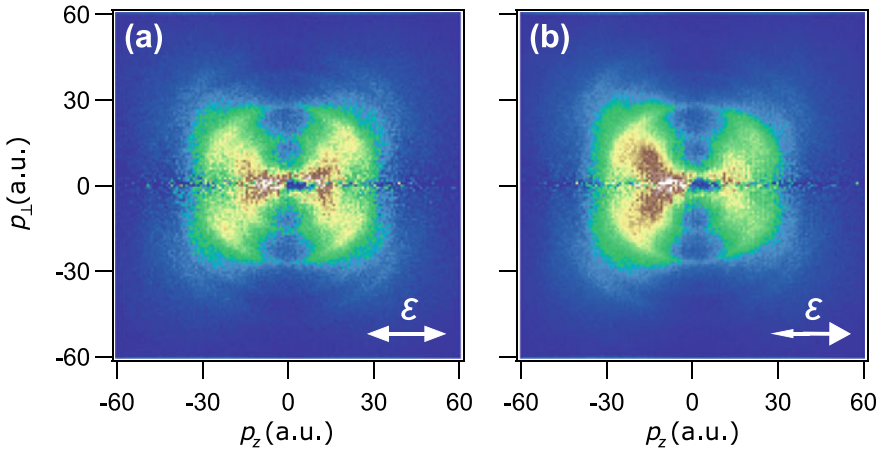

Fig. 6.9 Two-dimensional momentum images of the N^+ fragment ions produced in **a** one-color intense laser fields (45 fs, 800 nm, 1×10^{14} W/cm^2) and **b** phase-locked two-color intense laser fields (45 fs, 800 nm + 400 nm, 1×10^{14} W/cm^2, $I_{2\omega}/I_\omega = 0.04$, $\phi = 0.1\pi$). The momentum map represents a thin slice (with a slice width of ± 0.5 a.u.) of the three-dimensional momentum distribution in the plane containing the laser polarization direction denoted as ε. The momentum components parallel and perpendicular to the laser polarization direction are denoted with p_z and $p_\perp$, respectively. The arrow represents the direction of the larger amplitude. Adapted with permission from Ref. [24]. Copyright 2019 by American Physical Society

where $F_\omega(t)$ and $F_{2\omega}(t)$ are the envelope function of laser electric fields with the carrier frequency of ω and 2ω, and ϕ is the relative phase between two laser pulses. As shown in the inset of Fig. 6.8, phase-locked two-color laser fields have asymmetric electric field amplitudes, which can be controlled by changing the relative phase and the ratio between the intensity of each field, $I_{2\omega}/I_\omega$.

The N^+ momentum image obtained with phase-locked two-color intense laser fields (45 fs, 800 nm + 400 nm, 1×10^{14} W/cm^2, $I_{2\omega}/I_\omega = 0.04$, $\phi = 0.1\pi$ shows larger yields on the side of smaller electric field amplitude, while preserving the butterfly-like pattern as observed with the fundamental fields alone. The preferential ejection of N^+ fragments to the smaller amplitude side suggests that the tunneling ionization occurs more efficiently from the N atom side [56], whose electron density is larger than that on the O atom side as shown in Fig. 6.7.

The obtained ion images show concentric patterns associated with different dissociation pathways (see Fig. 6.10). Figure 6.11 shows fragment angular distributions for the $B^1\Pi$ component with the highest momentum ($|\mathbf{p}| \sim 50$ a.u.) [57]. The fragment distribution strongly depends on the shape of laser electric fields, and the fragment asymmetry is maximum at $\phi \sim 0$ or π when the laser field amplitude has the largest asymmetry.

To understand the origin of the phase dependence, theoretical calculations on tunneling ionization yields are carried out. According to the many electron weak-field asymptotic theory (ME-WFAT) [58], the tunneling ionization rate in a static

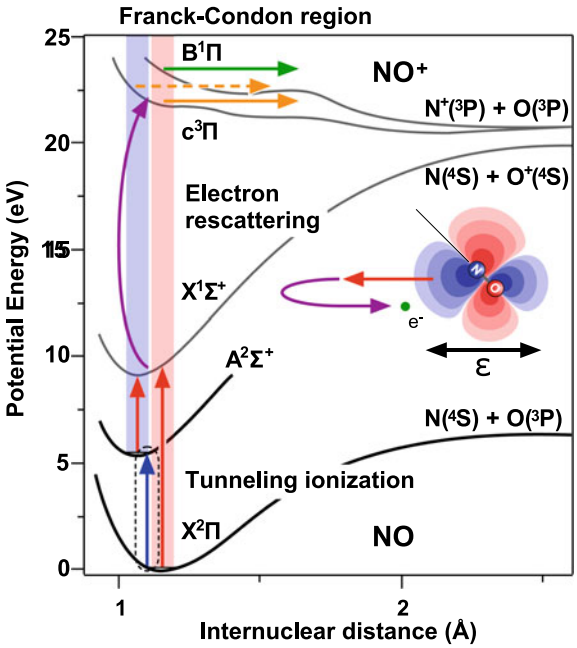

Fig. 6.10 Potential energy curves of the selected electronic states of NO and NO^+ [53–55]. Arrows schematically represent the dissociation pathways. Adapted with permission from Ref. [23]. Copyright 2016 by American Physical Society

electric field can be expressed as

$$G(\beta, F) = \left\{ |G_{00}(\beta)|^2 + \frac{F}{2\varkappa^2} \left[\left| G_{01}^{(+)}(\beta) \right|^2 + \left| G_{01}^{(-)}(\beta) \right|^2 \right] \right\} W_{00}(F), \tag{6.9}$$

where β is the angle between the molecular axis and the electric field, F is the amplitude of the electric field, $\varkappa = (2I_p)^{1/2}$ with I_p being the ionization potential. The structure factors G_{00} and G_{01} consist of factors determined by the molecular orbital of interest and the permanent dipole difference between neutral and ionic states. The field factor W_{00} is written as

$$W_{00}(F) = \frac{\varkappa}{2} \left(\frac{4\varkappa^2}{F} \right)^{2/-1} \exp\left(-\frac{2\varkappa^3}{3F} \right). \tag{6.10}$$

Here, the structure factors are obtained from the HOMO within the Hartree–Fock approximation using the X2DHF code in place of the Dyson orbital, which is good approximation for small diatomic molecules. The tunneling ionization yields are obtained from the calculated rates by time integration over the laser pulse. At $\phi = 0.1\pi$, the theoretical result exhibits a clear asymmetric butterfly-like structure with

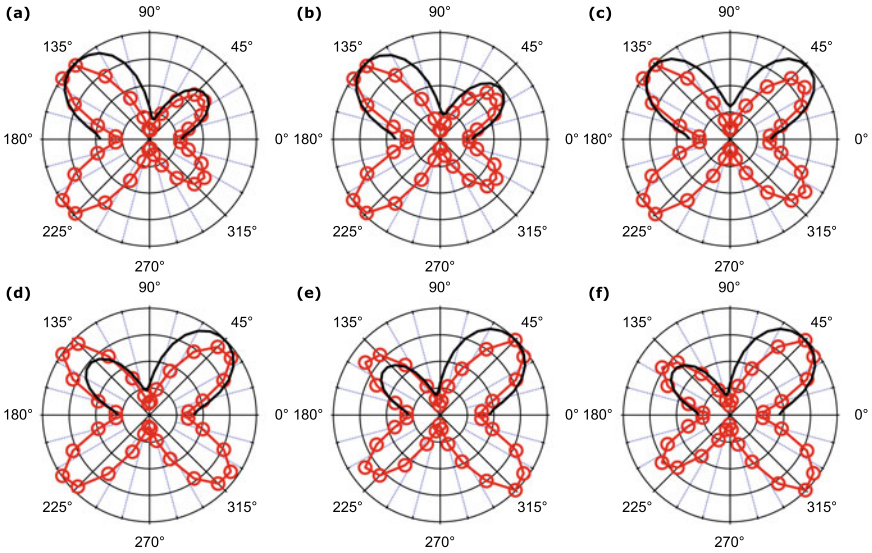

Fig. 6.11 The angular distributions of the $B^1\Pi$ dissociation components for different relative phases ϕ, **a** 0.1π, **b** 0.3π, **c** 0.5π, **d** 0.7π, **e** 0.9π and **f** 1.1π. The laser polarization direction is along the horizontal axis. Experimental results show clear dependence on the relative phase (red circles). Theoretical results obtained by ME-WFAT are shown in the first and second quadrants (solid line) for comparison. Adapted with permission from Ref. [24]. Copyright 2019 by American Physical Society

the larger peak at ~135° and the smaller peak at ~45°, as shown in Fig. 6.11a, in agreement with the experimental results.

The theoretical calculation reproduces the experimental phase dependence of the angular distribution, which shows a gradual variation of the asymmetry along the laser polarization direction, with the peak angles remaining essentially the same as shown in Fig. 6.11. The obtained results show that the fragment angular distribution is essentially governed by the shape of the outermost molecular orbital. It is worth noting that a counter intuitive angular dependence has been observed for OCS [15], where the large permanent dipole moment modifies effective ionization potentials depending on the molecular orientation. In the present case of NO, the experimental angular distribution has slightly narrower widths with peak angles slightly shifted towards the polarization axis compared with the theoretical results. These deviations could be attributed to the multi-orbital effects [59, 60] discussed to explain the angular distributions of the tunneling ionization of CO. In addition, the electron recollisional excitation involved in the dissociation process could also contribute. Since the molecular potential of NO^+ is anisotropic, the cross-section of electron impact excitation, $NO^+ + e^- \rightarrow N^+ + O + e^-$, is expected to vary with the orientation of the molecular ion, which results in the modification of the angular distribution of the fragment ions.

6.3.3 *Tunneling Ionization Imaging of Molecular Photoexcitation*

Presented here is tunneling ionization imaging in the first electronically excited state ($A^2\Sigma^+$) of NO, excited by a deep-UV (DUV) pulse of a wavelength of 226 nm. The electric configuration of the excited state is $\ldots(5\sigma)^2\ (1\pi)^4\ (2\pi)^0\ (3s\sigma)^1$, where an electron in the 2π orbital is promoted to the $3s\sigma$ orbital upon the photoexcitation (Fig. 6.12a). Here, 8-fs few-cycle intense laser pulses are used as probe pulses. The pump pulses are obtained by an optical parametric amplifier and its central wavelength is tuned to the A–X (0, 0) transition of NO. Since the amount of the $A^2\Sigma^+$ state is estimated to be only 0.5% of the $X^2\Pi$ state, an optical chopper is introduced to block the pump pulse in every other shot. The net signal from the excited state is obtained by subtraction of the pump alone and probe alone signals from the pump-probe signal.

The ion momentum images of N^+ fragments generated from the ground and excited states in the few-cycle intense laser fields (8 fs, 1.1×10^{14} W/cm^2) are

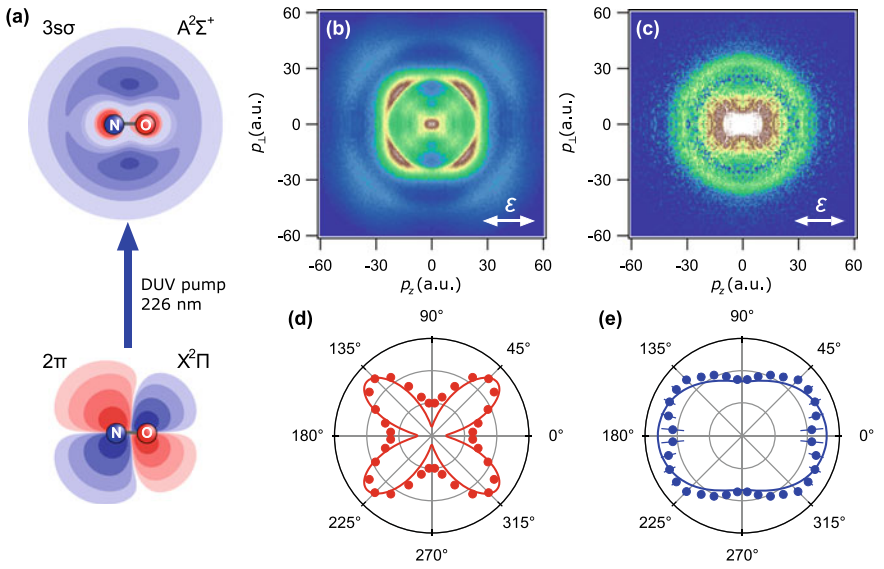

Fig. 6.12 **a** The highest occupied molecular orbitals, 2π and $3s\sigma$, in the $X^2\Pi$ and $A^2\Sigma^+$ states. Momentum images of the N^+ fragment ions produced by dissociative ionization starting from **b** the $X^2\Pi$ state and **c** the $A^2\Sigma^+$ state in few-cycle intense laser fields (8 fs, 1.1×10^{14} W/cm^2). Symmetries with respect to the p_z and $p_\perp$ axes are utilized to reduce the statistical uncertainty. The probe NIR laser polarization direction is denoted with ε. Polar plots of the fragment angular distributions obtained for **d** the $X^2\Pi$ and **e** $A^2\Sigma^+$ initial states. The distributions are evaluated on the $c^3\Pi$ dissociation components. Solid lines are theoretical tunneling ionization yields calculated by the ME-WFAT under the adiabatic approximation. Adapted with permission from Ref. [23]. Copyright 2016 by American Physical Society

shown in Fig. 6.12b, c. To improve the data statistics, the ion momentum images are symmetrized along the p_z and $p_\perp$ axes. For the ground state, clear peaks are observed at 45° with respect to the laser polarization direction as discussed in the previous section. Two distinct components appear at $|\mathbf{p}| = 25$ and 50 a.u., which are corresponding to the Franck–Condon dissociation via $c^3\Pi$ and $B^1\Pi$ states (see Fig. 6.10). Compared with the ion momentum images obtained with the 45 fs laser fields (Fig. 6.9), the image shows simple and sharp distributions due to suppression of post-ionization interaction with laser fields [23, 24].

Results for the excited state are shown in Fig. 6.12b, exhibiting a broad circular distribution around $|\mathbf{p}| = 32$ a.u. The increase of momentum is attributed to the shift of the Franck–Condon window to the steeper part of the $c^3\Pi$ potential, associated with the change in the equilibrium internuclear distance from 1.15 Å in $X^2\Pi$ state to 1.06 Å in $A^2\Sigma^+$ state [61]. The ion momentum image drastically changes by photoexcitation from 2π to $3s\sigma$ orbitals, showing that the fragment anisotropy reflects the changes in the shape of the outermost molecular orbital. The polar plots of the angular distribution of the N^+ fragments produced via the $c^3\Pi$ state are shown in Fig. 6.12d, e for the ground and excited states, respectively. Theoretical ionization yields calculated based on ME-WFAT show good agreement with the experimental results both for the ground and excited states. This presents that the fragment angular distribution reflects the tunneling ionization rates of the outermost molecular orbital and follows the change in the electron distribution in the molecular frame upon the photoexcitation from the 2π to $3s\sigma$ orbitals.

Finally, the excitation process to the dissociative state in NO^+ is discussed. To clarify the excitation process, the fragment yields via the $c^3\Pi$ state are measured as a function of the ellipticity of the probe laser pulse. The yields show the maximum at linear polarization and drastically decrease to reach near zero value with circular polarization for both the ground and excited states (Fig. 6.13). This ellipticity dependence suggests that electron rescattering associated with tunneling ionization is involved in the excitation to the $c^3\Pi$ state. For quantitative discussion, the ellipticity dependence is calculated by WFAT and adiabatic theory [23]. The calculated ellipticity dependence reproduced the experimental results for both of the ground and excited states, thus confirming the tunneling ionization followed by electron rescattering is responsible for dissociative ionization under the present experimental conditions. Since the ground state of NO^+ is singlet, electron impact excitation to triplet states may serve as a filter to favor tunneling rather than multiphoton ionization from the ground and excited states of NO.

In this section, our recent studies on molecular orbital imaging by laser tunneling ionization have been reviewed. The angular distribution of N^+ fragments produced by the dissociative ionization of NO, $NO \rightarrow NO^+ + e^- \rightarrow N^+ + O + e^-$ reflects changes in electron distribution in the molecular frame upon the photoexcitation of an electron, which can be considered as a model chemical reaction. Thanks to the ultrashort duration of intense laser pulses, the laser tunneling ionization provides a promising means towards the tracking of ultrafast electron dynamics during chemical reaction processes.

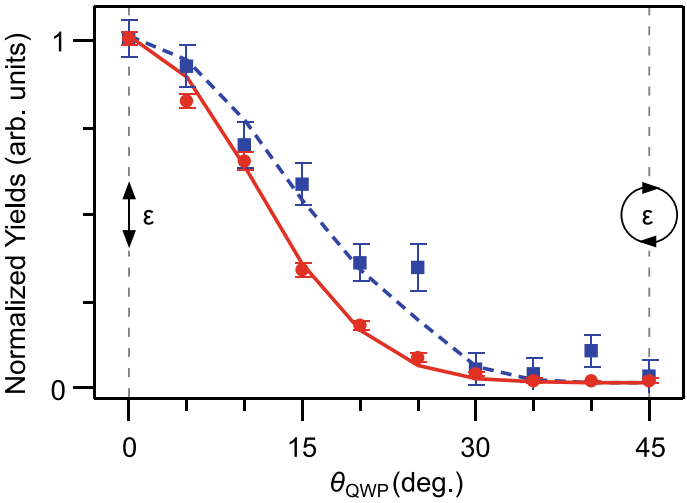

Fig. 6.13 Relative yields of the $c^3\Pi$ dissociation components as a function of the angle of a quarter-wave plate θ_{QWP} with the $X^2\Pi$ (red circles) and $A^2\Sigma^+$ (blue squares) states of NO as the initial state. The solid line is a result of the least-square fitting to the experimental data for the ground state, while the dashed line represents a theoretical prediction for the excited state. Adapted with permission from Ref. [23]. Copyright 2016 by American Physical Society

6.4 Summary and Outlook

Two types of time-resolved molecular orbital imaging techniques have been discussed in this chapter, both of which would open the door to the investigation of the driving force behind chemical reaction. One is TR-EMS and the other is the laser tunneling ionization imaging. It is shown that TR-EMS has the distinctive feature in its potential capability to observe not only the HOMO but also all other, more tightly bound orbitals of a transient, evolving system during chemical reaction, with the rigorous orbital selection based on the energy conservation law. It is the advantage of TR-EMS that the well-established knowledge about the electron-molecule collision dynamics for traditional EMS can be applied in a straightforward fashion to the time-resolved measurements of chemical reaction in a laser-field-free condition. However, there is ample room for improvements, mainly in data statistics and energy and time resolution. These have to be improved by introducing the ever-developing technologies that provide more intense laser, electron and molecular beams [33].

The ultrafast laser tunneling imaging technique can offer a unique approach to visualize the dynamics of outermost electrons of molecules, with a high temporal resolution in tens of femtoseconds or shorter. On the other hand, it is necessary to take into account various factors contributing laser tunneling ionization, such as dipole moment and multielectron effects, for proper interpretation of obtained images. Further investigation of laser tunneling ionization process needs to be performed for general applications.

The qualitative difference between TR-EMS and the laser tunneling ionization imaging is that the former looks at a molecular orbital in momentum space while the latter in position space. On the other hand, the common strong point of the two techniques is that they are both sensitive to the behavior of electron moving around the outer region of a transient, evolving system, far from the nuclei, which governs its reactivity. These similarity and dissimilarity of the two techniques ensure that future work on why the atoms are dancing in such a way, which is at the heart of chemical reaction dynamics, will be tackled from multiple perspectives, when their paths are crossed.

Acknowledgements MY and MT thank the technical staff of the machine shop at the Institute of Multidisciplinary Research for Advanced Materials and of the equipment development center at the Institute for Molecular Science for their expertise and skills in development of the TR-EMS apparatus. MT acknowledges financial support by JSPS KAKENHI Grant Numbers 20225001, 25248002 and 17F17338, and a support by MEXT Five-star Alliance Program. MY acknowledges financial support by JSPS KAKENHI Grant Numbers 21750005 and 15H03762, and by the Sumitomo Foundation and the Yamada Science Foundation. TE and AH are grateful to Prof. Oleg. I. Tolstikhin (MIPT, Russia) and Prof. Toru Morishita (UEC, Japan) for theoretical calculations on laser tunneling ionization imaging of NO. AH acknowledges financial support by JSPS KAKENHI Grant Numbers 19H00887 and 16H04029, MEXT Quantum Leap Flagship Program (MEXT Q-LEAP) Grant Number JPMXS0118068681 and by World Research Unit (B-1) of Reaction Infography (R-ing) at Nagoya University. TE acknowledges Grant-in-Aid for JSPS fellows (25 2966).

References

1. R.C. Evans, P. Douglas, H.D. Burrows (eds.), *Applied Photochemistry* (Springer, New York, 2013)
2. K. Fukui, Role of frontier orbitals in chemical reactions. Science **218**, 747–754 (1982). https://doi.org/10.1126/science.218.4574.747
3. A. Stolow, A.E. Bragg, D.M. Neumark, Femtosecond time-resolved photoelectron spectroscopy. Chem. Rev. **104**, 1719–1757 (2004). https://doi.org/10.1021/cr020683w
4. T. Suzuki, Femtosecond time-resolved photoelectron imaging. Annu. Rev. Phys. Chem. **57**, 555–592 (2006). https://doi.org/10.1146/annurev.physchem.57.032905.104601
5. J.C. Tully, Molecular dynamics with electronic transitions. J. Chem. Phys. **93**, 1061–1071 (1990). https://doi.org/10.1063/1.459170
6. C.-Y. Zhu, H. Nakamura, The two-state linear curve crossing problems revisited. II. Analytical approximations for the Stokes constant and scattering matrix: The Landau–Zener case. J. Chem. Phys. **97**, 8497–8514 (1992).https://doi.org/10.1063/1.463368
7. I.E. McCarthy, E. Weigold, (e, 2e) spectroscopy. Phys. Rep. **27**, 275–371 (1976)
8. C.E. Brion, Looking at orbitals in the laboratory: the experimental investigation of molecular wavefunctions and binding energies by electron momentum spectroscopy. Int. J. Quantum Chem. **29**, 1397–1428 (1986). https://doi.org/10.1002/qua.560290534
9. K.T. Leung, in *Theoretical Models of Chemical Bonding, Part 3*. ed. by Z.B. Maksic (Springer, Berlin, 1991), p.339
10. M.A. Coplan, J.H. Moor, J.P. Doering, (e, 2e) spectroscopy. Rev. Mod. Phys. **66**, 985–1014 (1994). https://doi.org/10.1103/RevModPhys.66.985
11. E. Weigold, I.E. McCarthy, *Electron Momentum Spectroscopy* (Kluwer Academic/Plenum, New York, 1999)

12. V.G. Neudachin, Y.V. Popov, Y.F. Smirnov, Electron momentum spectroscopy of atoms, molecules and thin films. Phys. Usp. **42**, 1017–1044 (1999). https://doi.org/10.1070/PU1999v042n10ABEH000492
13. M. Takahashi, Looking at molecular orbitals in three-dimensional form: from dream to reality. Bull. Chem. Soc. Jpn **82**, 751–777 (2009). https://doi.org/10.1246/bcsj.82.751
14. D. Pavičić, K.F. Lee, D.M. Rayner, P.B. Corkum, D.M. Villeneuve, Direct measurement of the angular dependence of ionization for N_2, O_2, and CO_2 in intense laser fields. Phys. Rev. Lett. **98**, 243001 (2007). https://doi.org/10.1103/PhysRevLett.98.243001
15. L. Holmegaard, J.L. Hansen, L. Kalhøj, S. Louise Kragh, H. Stapelfeldt, F. Filsinger, J. Küpper, G. Meijer, D. Dimitrovski, M. Abu-samha, C.P.J. Martiny, L. Bojer Madsen, Photoelectron angular distributions from strong-field ionization of oriented molecules. Nat. Phys. **6**, 428–432 (2010). https://doi.org/10.1038/nphys1666
16. J.L. Hansen, L. Holmegaard, L. Kalhøj, S.L. Kragh, H. Stapelfeldt, F. Filsinger, G. Meijer, J. Küpper, D. Dimitrovski, M. Abu-samha, C.P.J. Martiny, L.B. Madsen, Ionization of one- and three-dimensionally-oriented asymmetric-top molecules by intense circularly polarized femtosecond laser pulses. Phys. Rev. A **83**, 023406 (2011). https://doi.org/10.1103/PhysRevA.83.023406
17. A. Staudte, S. Patchkovskii, D. Pavičić, H. Akagi, O. Smirnova, D. Zeidler, M. Meckel, D.M. Villeneuve, R. Dörner, M.Y. Ivanov, P.B. Corkum, Angular tunneling ionization probability of fixed-in-space H_2 molecules in intense laser pulses. Phys. Rev. Lett. **102**, 033004 (2009). https://doi.org/10.1103/PhysRevLett.102.033004
18. H. Akagi, T. Otobe, A. Staudte, A. Shiner, F. Turner, R. Dörner, D.M. Villeneuve, P.B. Corkum, Laser tunnel ionization from multiple orbitals in HCl. Science **325**, 1364–1367 (2009). https://doi.org/10.1126/science.1175253
19. J. Wu, L.P.H. Schmidt, M. Kunitski, M. Meckel, S. Voss, H. Sann, H. Kim, T. Jahnke, A. Czasch, R. Dörner, Multiorbital tunneling ionization of the CO molecule. Phys. Rev. Lett. **108**, 183001 (2012). https://doi.org/10.1103/PhysRevLett.108.183001
20. A.S. Alnaser, S. Voss, X.M. Tong, C.M. Maharjan, P. Ranitovic, B. Ulrich, T. Osipov, B. Shan, Z. Chang, C.L. Cocke, Effects of molecular structure on ion disintegration patterns in ionization of O_2 and N_2 by short laser pulses. Phys. Rev. Lett. **93**, 113003 (2004). https://doi.org/10.1103/PhysRevLett.93.113003
21. A.S. Alnaser, C.M. Maharjan, X.M. Tong, B. Ulrich, P. Ranitovic, B. Shan, Z. Chang, C.D. Lin, C.L. Cocke, I.V. Litvinyuk, Effects of orbital symmetries in dissociative ionization of molecules by few-cycle laser pulses. Phys. Rev. A **71**, 031403(R) (2005). https://doi.org/10.1103/PhysRevA.71.031403
22. I. Znakovskaya, P. von den Hoff, S. Zherebtsov, A. Wirth, O. Herrwerth, M.J.J. Vrakking, R. de Vivie-Riedle, M.F. Kling, Attosecond control of electron dynamics in carbon monoxide. Phys. Rev. Lett. **103**, 103002 (2009). https://doi.org/10.1103/PhysRevLett.103.103002
23. T. Endo, A. Matsuda, M. Fushitani, T. Yasuike, O.I. Tolstikhin, T. Morishita, A. Hishikawa, Imaging electronic excitation of NO by ultrafast laser tunneling ionization. Phys. Rev. Lett. **116**, 163002 (2016). https://doi.org/10.1103/PhysRevLett.116.163002
24. T. Endo, H. Fujise, H. Hasegawa, A. Matsuda, M. Fushitani, O.I. Tolstikhin, T. Morishita, A. Hishikawa, Angle dependence of dissociative tunneling ionization of NO in asymmetric two-color intense laser fields. Phys. Rev. A **100**, 053422 (2019). https://doi.org/10.1103/PhysRevA.100.053422
25. J. Itatani, J. Levesque, D. Zeidler, H. Niikura, H. Pépin, J.C. Kieffer, P.B. Corkum, D.M. Villeneuve, Tomographic imaging of molecular orbitals. Nature **432**, 867–871 (2004). https://doi.org/10.1038/nature03183
26. H.J. Wörner, J.B. Bertrand, D.V. Kartashov, P.B. Corkum, D.M. Villeneuve, Following a chemical reaction using high-harmonic interferometry. Nature **466**, 604–607 (2010). https://doi.org/10.1038/nature09185
27. P.M. Kraus, H.J. Wörner, Time-resolved high-harmonic spectroscopy of valence electron dynamics. Chem. Phys. **414**, 32–44 (2013). https://doi.org/10.1016/j.chemphys.2012.01.013

28. W. Li, X. Zhou, R. Lock, S. Patchkovskii, A. Stolow, H.C. Kapteyn, M.M. Murnane, Time-resolved dynamics in N_2O_4 probed using high harmonic generation. Science **322**, 1207–1211 (2008). https://doi.org/10.1126/science.1163077
29. Y. Zheng, I.E. McCarthy, E. Weigold, D. Zhang, Direct observation of the momentum-density profile of excited and oriented sodium atoms. Phys. Rev. Lett. **64**, 1358–1360 (1990). https://doi.org/10.1103/PhysRevLett.64.1358
30. M. Yamazaki, H. Satoh, M. Ueda, D.B. Jones, Y. Asano, N. Watanabe, A. Czasch, O. Jagutzki, M. Takahashi, A highly sensitive electron momentum spectrometer incorporating a multiparticle imaging detector. Meas. Sci. Technol. **22**, 075602-1–075602-13 (2011). https://doi.org/10.1088/0957-0233/22/7/075602
31. Q.G. Tian, K.D. Wang, X. Shan, X.J. Chen, A high-sensitivity angle and energy dispersive multichannel electron momentum spectrometer with 2π angle range. Rev. Sci. Instrum. **82**, 033110-1–033110-7 (2011). https://doi.org/10.1063/1.3568744
32. M. Yamazaki, Y. Kasai, K. Oishi, H. Nakazawa, M. Takahashi, Development of an (e, 2e) electron momentum spectroscopy apparatus using an ultrashort pulsed electron gun. Rev. Sci. Instrum. **84**, 063105-1–063105-10 (2013). https://doi.org/10.1063/1.4809792
33. M. Yamazaki, Y. Kasai, K. Oishi, H. Nakazawa, M. Takahashi, Development of time-resolved (e, 2e) electron momentum spectroscopy: a tool for visualizing the motion of electrons during a chemical reaction. J. Phys. Conf. Ser. **488**, 012056-1–012056-6 (2014). https://doi.org/10.1088/1742-6596/488/1/012056
34. Y. Tang, X. Shan, Z. Liu, S. Niu, E. Wang, X. Chen, Development of an electron momentum spectrometer for time-resolved experiments employing nanosecond pulsed electron beam. Rev. Sci. Instrum. **89**, 033101-1–033101-8 (2018). https://doi.org/10.1063/1.5018665
35. J.C. Williamson, A.H. Zewail, Ultrafast electron diffraction. Velocity mismatch and temporal resolution in crossed-beam experiments. Chem. Phys. Lett. **209**, 10–16 (1993). https://doi.org/10.1016/0009-2614(93)87193-7
36. M. Yamazaki, K. Oishi, H. Nakazawa, C.Y. Zhu, M. Takahashi, Molecular orbital imaging of the acetone S_2 excited state using time-resolved (e, 2e) electron momentum spectroscopy. Phys. Rev. Lett. **114**, 103005-1–103005-5 (2015). https://doi.org/10.1103/PhysRevLett.114.103005
37. J.C. Owrutsky, A.P. Baronavski, Ultrafast photodissociation dynamics of the S_1 and S_2 states of acetone. J. Chem. Phys. **110**, 11206–11213 (1999). https://doi.org/10.1063/1.478003
38. E. Gibney, Nature **519**, 392 (2015). https://doi.org/10.1038/519392d
39. T. Wogan, Physics **8**, 23 (2015). https://doi.org/10.1103/Physics.8.23
40. M. Yamazaki, Y. Tang, M. Takahashi, Ionization propensity and electron momentum distribution of the toluene S_1 excited state studied by time-resolved binary (e, 2e) spectroscopy. Phys. Rev. A **94**, 052509-1–052509-5 (2016). https://doi.org/10.1103/PhysRevA.94.052509
41. C.G. Hickman, J.R. Gascooke, W.D. Lawrance, The S_1–S_0 ($^1B_2$–$^1A_1$) transition of jet-cooled toluene: excitation and dispersed fluorescence spectra, fluorescence lifetimes, and intramolecular vibrational energy redistribution. J. Chem. Phys. **104**, 4887–4901 (1996). https://doi.org/10.1063/1.471122
42. H. Nakatsuji, Description of two- and many-electron processes by the SAC-CI method. Chem. Phys. Lett. **177**, 331–337 (1991). https://doi.org/10.1016/0009-2614(91)85040-4
43. X.M. Tong, Z.X. Zhao, C.D. Lin, Theory of molecular tunneling ionization. Phys. Rev. A **66**, 033402 (2002). https://doi.org/10.1103/PhysRevA.66.033402
44. O.I. Tolstikhin, T. Morishita, L.B. Madsen, Theory of tunneling ionization of molecules: weak-field asymptotics including dipole effects. Phys. Rev. A **84**, 053423 (2011). https://doi.org/10.1103/PhysRevA.84.053423
45. S. Petretti, Y.V. Vanne, A. Saenz, A. Castro, P. Decleva, Alignment-dependent ionization of N_2, O_2, and CO_2 in intense laser fields. Phys. Rev. Lett. **104**, 223001 (2010). https://doi.org/10.1103/PhysRevLett.104.223001
46. T. Otobe, K. Yabana, J.-I. Iwata, First-principles calculations for the tunnel ionization rate of atoms and molecules. Phys. Rev. A **69**, 053404 (2004). https://doi.org/10.1103/PhysRevA.69.053404

47. B. Zhang, J. Yuan, Z. Zhao, Dynamic core polarization in strong-field ionization of CO molecules. Phys. Rev. Lett. **111**, 163001 (2013). https://doi.org/10.1103/PhysRevLett.111.163001
48. A. Hishikawa, E.J. Takahashi, A. Matsuda, Electronic and nuclear responses of fixed-in-space H_2S to ultrashort intense laser fields. Phys. Rev. Lett. **97**, 243002 (2006). https://doi.org/10.1103/PhysRevLett.97.243002
49. H. Ohmura, N. Saito, T. Morishita, Molecular tunneling ionization of the carbonyl sulfide molecule by double-frequency phase-controlled laser fields. Phys. Rev. A **89**, 013405 (2014). https://doi.org/10.1103/PhysRevA.89.013405
50. T. Endo, H. Fujise, A. Matsuda, M. Fushitani, H. Kono, A. Hishikawa, Coincidence momentum imaging of asymmetric Coulomb explosion of CO_2 in phase-locked two-color intense laser fields. J. Electron Spectrosc. Relat. Phenom. **207**, 50–54 (2016). https://doi.org/10.1016/j.elspec.2015.12.010
51. T. Endo, H. Fujise, Y. Kawachi, A. Ishihara, A. Matsuda, M. Fushitani, H. Kono, A. Hishikawa, Selective bond breaking of CO_2 in phase-locked two-color intense laser fields: laser field intensity dependence. Phys. Chem. Chem. Phys. **19**, 3550–3556 (2017). https://doi.org/10.1039/C6CP07471E
52. D. Ray, F. He, S. De, W. Cao, H. Mashiko, P. Ranitovic, K.P. Singh, I. Znakovskaya, U. Thumm, G.G. Paulus, M.F. Kling, I.V. Litvinyuk, C.L. Cocke, Ion-energy dependence of asymmetric dissociation of D_2 by a two-color laser field. Phys. Rev. Lett. **103**, 223201 (2009). https://doi.org/10.1103/PhysRevLett.103.223201
53. F.R. Gilmore, Potential energy curves for N_2, NO, O_2 and corresponding ions. J. Quant. Spectrosc. Radiat. Transfer **5**, 369–389 (1965). https://doi.org/10.1016/0022-4073(65)90072-5
54. D.L. Albritton, A.L. Schmeltekopf, R.N. Zare, Potential energy curves for NO^+. J. Chem. Phys. **71**, 3271 (1979). https://doi.org/10.1063/1.438757
55. H. Partridge, S.R. Langhoff, C.W. Bauschlicher Jr., Theoretical study of the spectroscopy of NO^+. J. Chem. Phys. **93**, 7179 (1990). https://doi.org/10.1063/1.459716
56. H. Li, D. Ray, S. De, I. Znakovskaya, W. Cao, G. Laurent, Z. Wang, M.F. Kling, A.T. Le, C.L. Cocke, Orientation dependence of the ionization of CO and NO in an intense femtosecond two-color laser field. Phys. Rev. A **84**, 043429 (2011). https://doi.org/10.1103/PhysRevA.84.043429
57. A. Lafosse, M. Lebech, J.C. Brenot, P.M. Guyon, O. Jagutzki, L. Spielberger, M. Vervloet, J.C. Houver, D. Dowek, Vector correlations in dissociative photoionization of diatomic molecules in the VUV range: strong anisotropies in electron emission from spatially oriented NO molecules. Phys. Rev. Lett. **84**, 5987 (2000). https://doi.org/10.1103/PhysRevLett.84.5987
58. O.I. Tolstikhin, L.B. Madsen, T. Morishita, Weak-field asymptotic theory of tunneling ionization in many-electron atomic and molecular systems. Phys. Rev. A **89**, 013421 (2014). https://doi.org/10.1103/PhysRevA.89.013421
59. S. Ohmura, T. Kato, T. Oyamada, S. Koseki, H. Ohmura, H. Kono, A single-electron picture based on the multiconfiguration time-dependent Hartree-Fock method: application to the anisotropic ionization and subsequent high-harmonic generation of the CO molecule. J. Phys. B **51**, 034001 (2018). https://doi.org/10.1088/1361-6455/aa9e45
60. V.P. Majety, A. Scrinzi, Static field ionization rates for multi-electron atoms and small molecules. J. Phys. B **48**, 245603 (2015). https://doi.org/10.1088/0953-4075/48/24/245603
61. G. Herzberg, *Spectra of Diatomic Molecules*, 2nd edn. (Van Nostrand, New York, 1950), p.558